Supplementary Information

Interpenetrating Gels as Conducting/Adhering Matrices Enabling High-Performance Silicon Anodes

Tingting Xia,[§] Chengfei Xu,[§] Pengfei Dai, Xiaoyun Li, Riming Lin, Yawen Tang, Yiming Zhou and Ping Wu*

Jiangsu Key Laboratory of New Power Batteries, Jiangsu Collaborative Innovation Center of Biomedical Functional Materials, School of Chemistry and Materials Science, Nanjing Normal University, Nanjing 210023 (China)

*E-mail: zjuwuping@njnu.edu.cn (P.W.).

[§] These authors contributed equally to this work.

EXPERIMENTAL SECTION

Chemicals and materials. Polyvinyl alcohol (PVA, degree of polymerization, 1750 ± 50), glutaraldehyde (GA, 50% aqueous solution), pyrrole, ammonium persulfate (APS), and copper phthalocyanine-3,4',4'',4'''-tetrasulfonic acid tetrasodium salt (CuPcTs) were bought from Sigma-Aldrich. Commercial Si particle (average size of ~50 nm) was obtained from Alfa Aesar.

Synthesis of the PPy/PVA interpenetrating gel. In a typical synthesis, 1 mL 25% GA aqueous solution, 152 μL pyrrole, and 3 mg CuPcTs were added and dissolved in 10 mL 2 wt% PVA aqueous solution. Then, 3 mL 1 M APS aqueous solution was added into the above solution, and the reaction system was carried out for 2 h. Subsequently, the obtained gel was immersed into deionized water to remove unreacted and generated ions, yielding the PPy/PVA interpenetrating hydrogel. The PPy/PVA hydrogel was further freeze-dried to obtain PPy/PVA interpenetrating aerogel.

Synthesis of the Si@PPy/PVA gel electrode. For the electrode preparation, 0.6 g commercial Si particle was added to the gel precursor solution and *in situ* immobilized within the PPy/PVA interpenetrating gel during the gelation processes. Subsequently, the as-prepared Si@PPy/PVA hybrid gel was spread on copper foil current collectors, and then the electrode foil was immersed into deionized water to remove unreacted/generated ions and then dried in a vacuum oven at 90 °C for 12 h.

Characterization. The crystalline phases and crystallinity of the as-prepared samples were examined by X-ray powder diffraction (XRD) with a Cu Kα radiation (Rigaku D/max 2500/PC). The morphology and microstructure of the products were investigated by scanning electron microscope (SEM, JSM-5610LV), and high-resolution transmission electron microscopy (HRTEM, JEOL JEM-2010F, 200 kV) accompanied by energy-dispersive X-ray spectrometer (EDS, Thermo Fisher Scientific). Fourier transform infrared (FTIR) spectroscopy was conducted by a Bruker Tensor 27

spectrometer. Nitrogen adsorption/desorption tests were performed using a Micromeritics ASAP 2460 analyzer, and Brunauer-Emmett-Teller (BET) and Barrett-Joyner-Halenda (BJH) methods were used to measure surface area, pore volume, and pore size, respectively. Thermogravimetric analysis (TGA) was conducted on a thermal analyzer (NETZSCH STA) at a heating rate of 10 °C min^{-1} under air atmosphere.

Electrochemical measurement. The electrochemical performances toward lithium storage were tested using CR2025 coin cells, which were assembled in an Innovative Technology glove box (IL-2GB). The as-obtained Si@PPy/PVA gel electrode was used as working electrode, and as a control sample, the conventional electrode was prepared by spreading aqueous slurry, containing 70 wt% commercial Si particle, 15 wt% carbon black (CB), and 15 wt% sodium carboxymethyl-cellulose (CMC), on copper foils. Only silicon component was considered as active material when calculating the specific capacities of the gel electrode and conventional electrode. The counter/reference electrode was lithium foil, and the electrolyte was 1 M $LiPF_6$ in ethylene carbonate and dimethyl carbonate (1:1 in volume) containing 5 vol% fluoroethylene carbonate. The charge/discharge behaviors of the gel electrode and conventional electrode were investigated using a LANHE CT2001A battery tester (0.01-1.2 V, 0.1 A g^{-1} in the first cycle and 0.5 to 5 A g^{-1} in subsequent cycles).

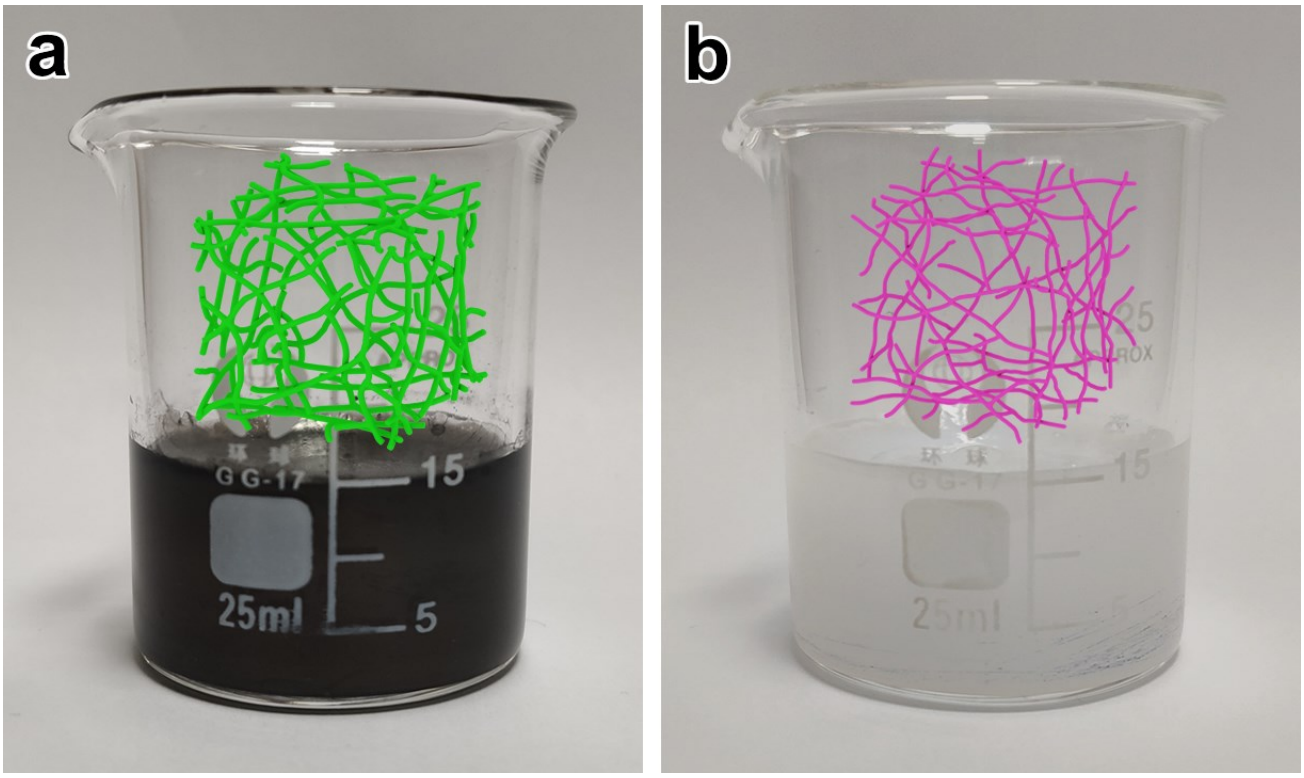

Fig. S1 Photographs of the PPy hydrogel (a), PVA hydrogel (b), and their corresponding models (insets).

Synthesis of the PPy hydrogel: 152 μL pyrrole and 3 mg CuPcTs were dissolved in 11 mL deionized water. Then, 3 mL 1 M APS aqueous solution was added into the above solution, yielding the PPy hydrogel.

Synthesis of the PVA hydrogel: 1 mL 25% GA aqueous solution were added in 10 mL 2 wt% PVA aqueous solution. Then, 3 mL 1.5 M HCl aqueous solution was added into the above solution, yielding the PVA hydrogel.

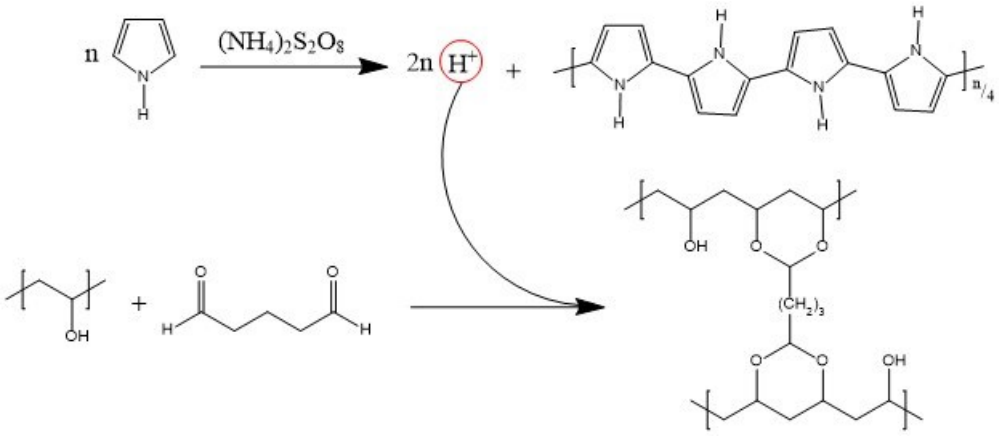

Fig. S2 The detailed reaction equations for the simultaneous and correlative gelation reactions of the PPy/PVA interpenetrating gel.

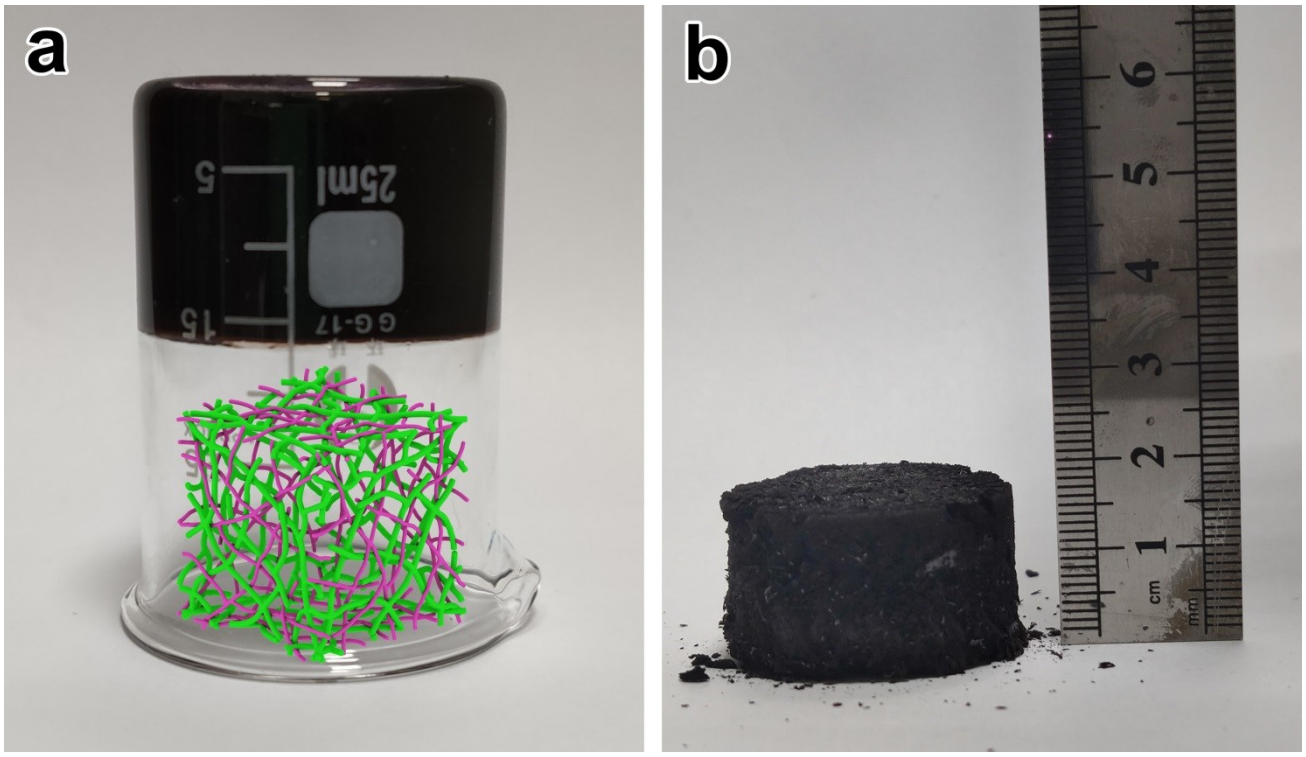

Fig. S3 Photographs of the PPy/PVA interpenetrating hydrogel (a) and aerogel (b).

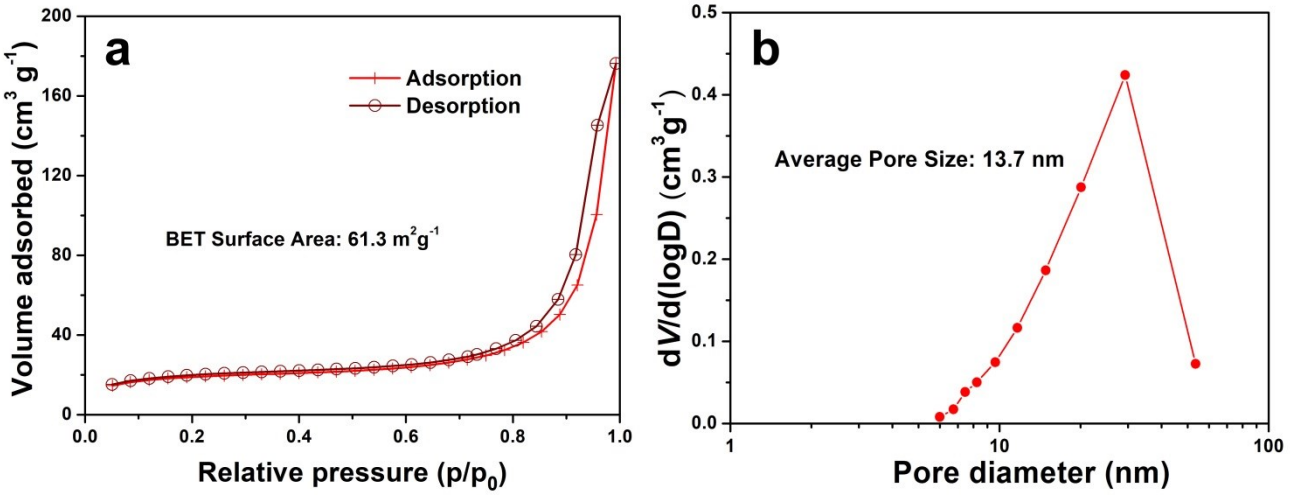

Fig. S4 Nitrogen adsorption/desorption isotherms (a) and pore size distribution (b) of the PPy/PVA interpenetrating gel.

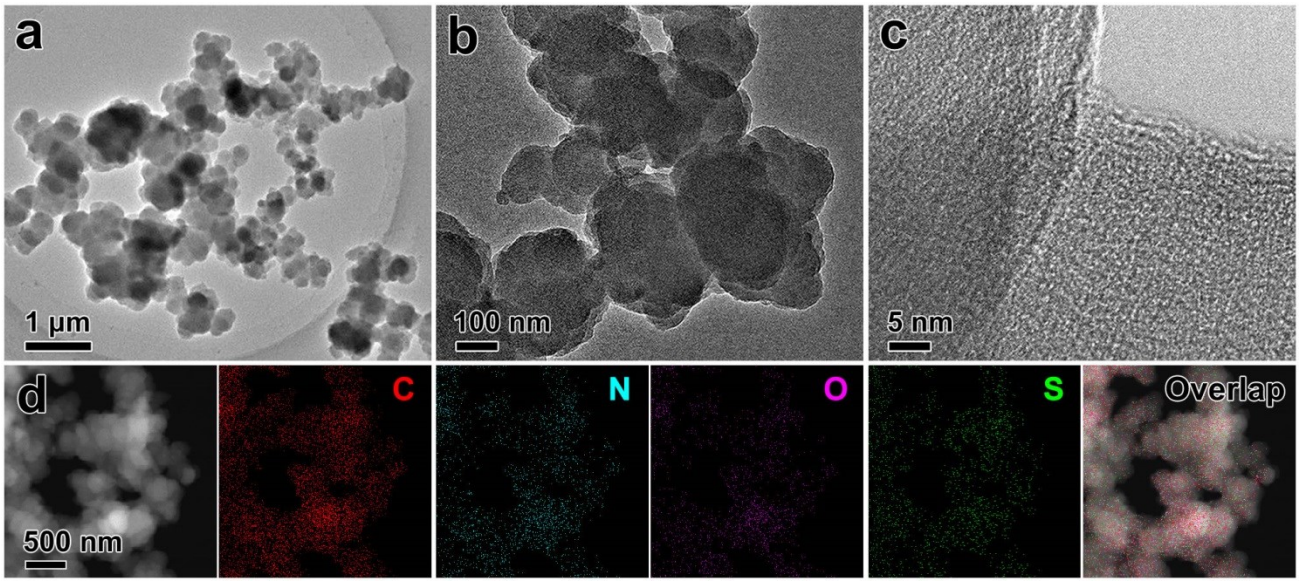

Fig. S5 (a-c) TEM images and (d) STEM-EDS elemental mappings of the PPy gel.

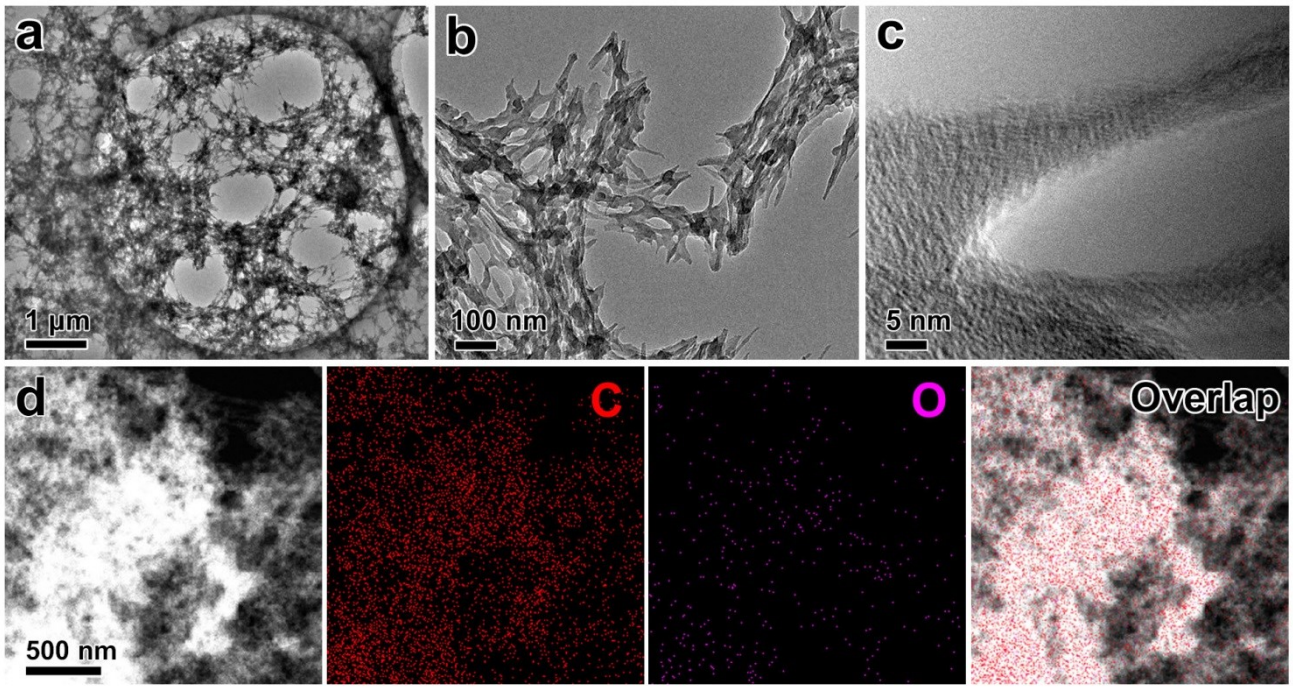

Fig. S6 (a-c) TEM images and (d) STEM-EDS elemental mappings of the PVA gel.

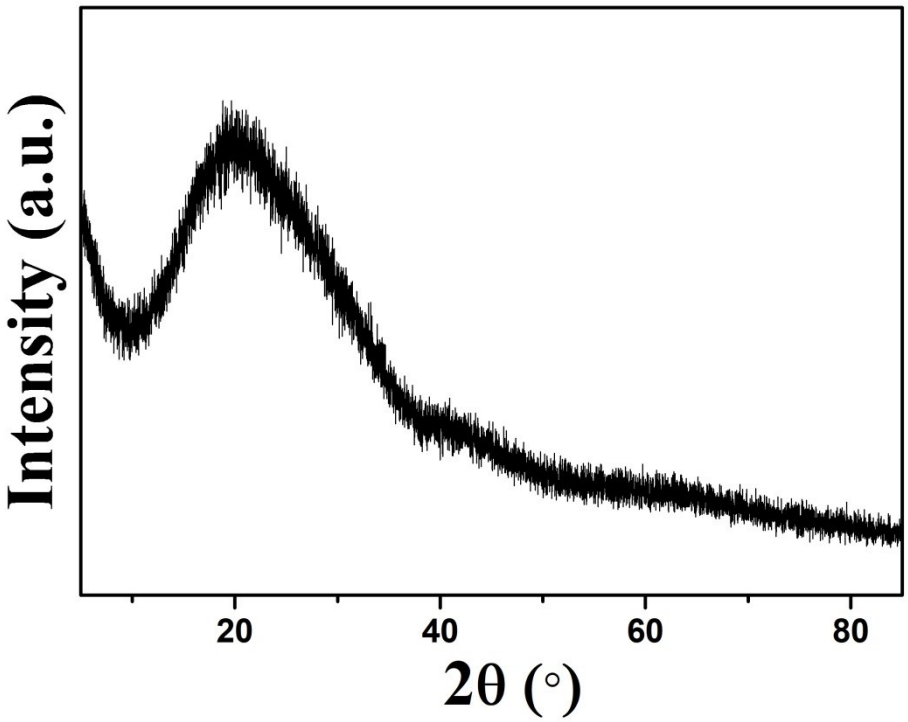

Fig. S7 XRD pattern of the the PPy/PVA interpenetrating gel.

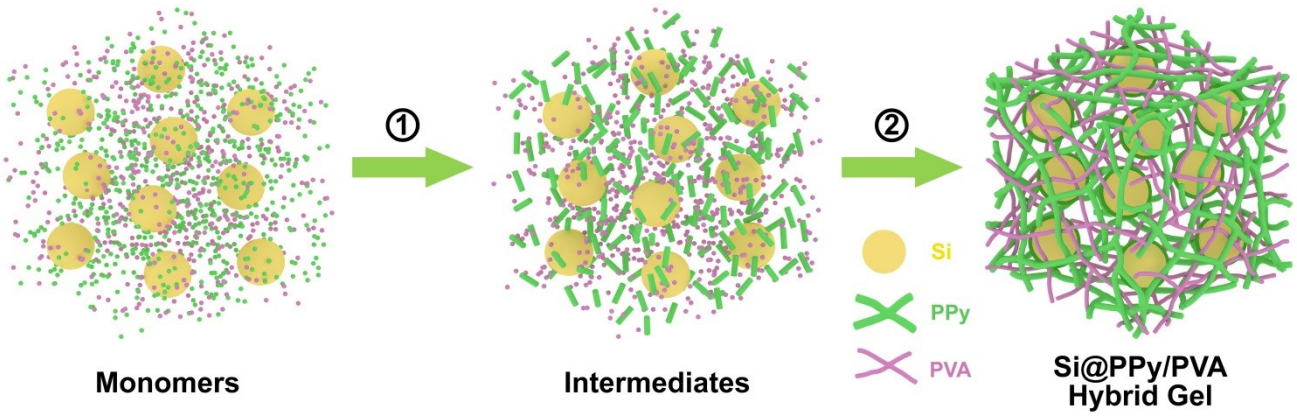

Fig. S8 Synthetic diagram of the Si@PPy/PVA hybrid gel.

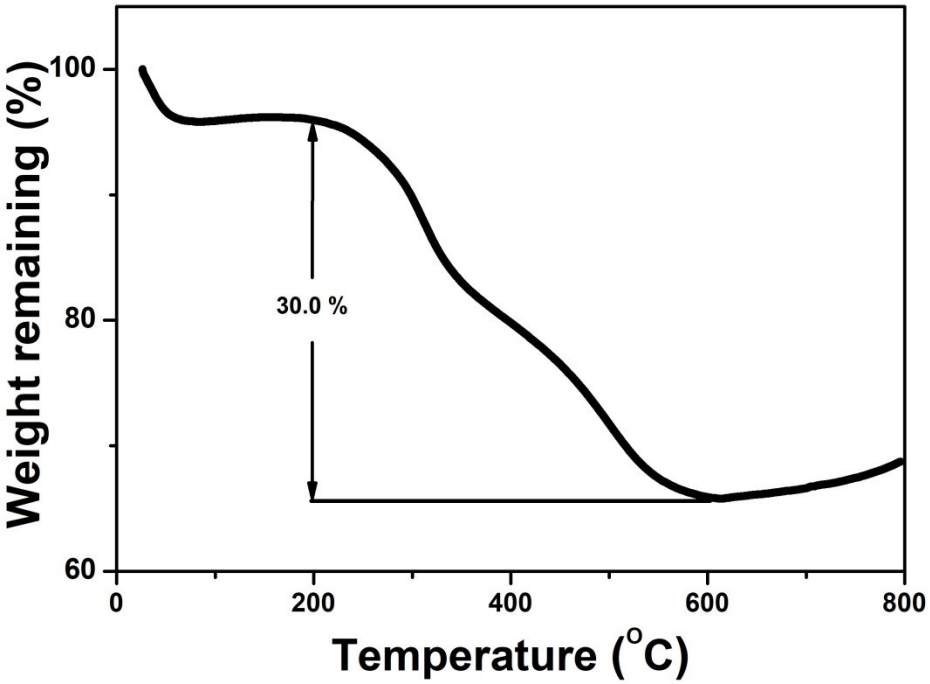

Fig. S9 TGA curve of the Si@PPy/PVA hybrid gel.

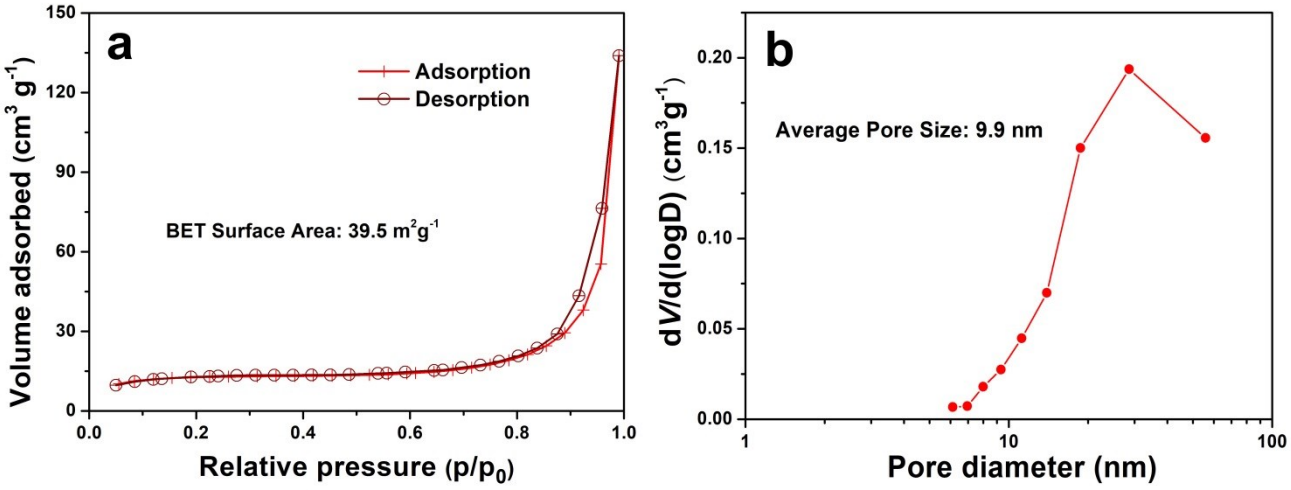

Fig. S10 Nitrogen adsorption/desorption isotherms (a) and pore size distribution (b) of the Si@PPy/PVA hybrid gel.

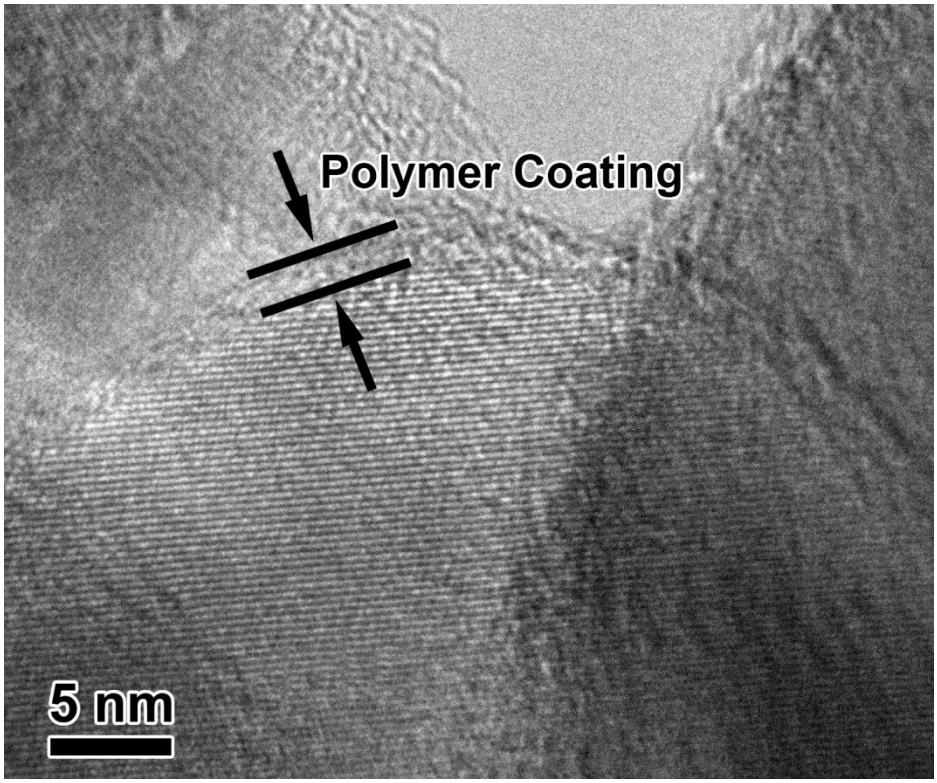

Fig. S11 HRTEM image of the Si@PPy/PVA hybrid gel.

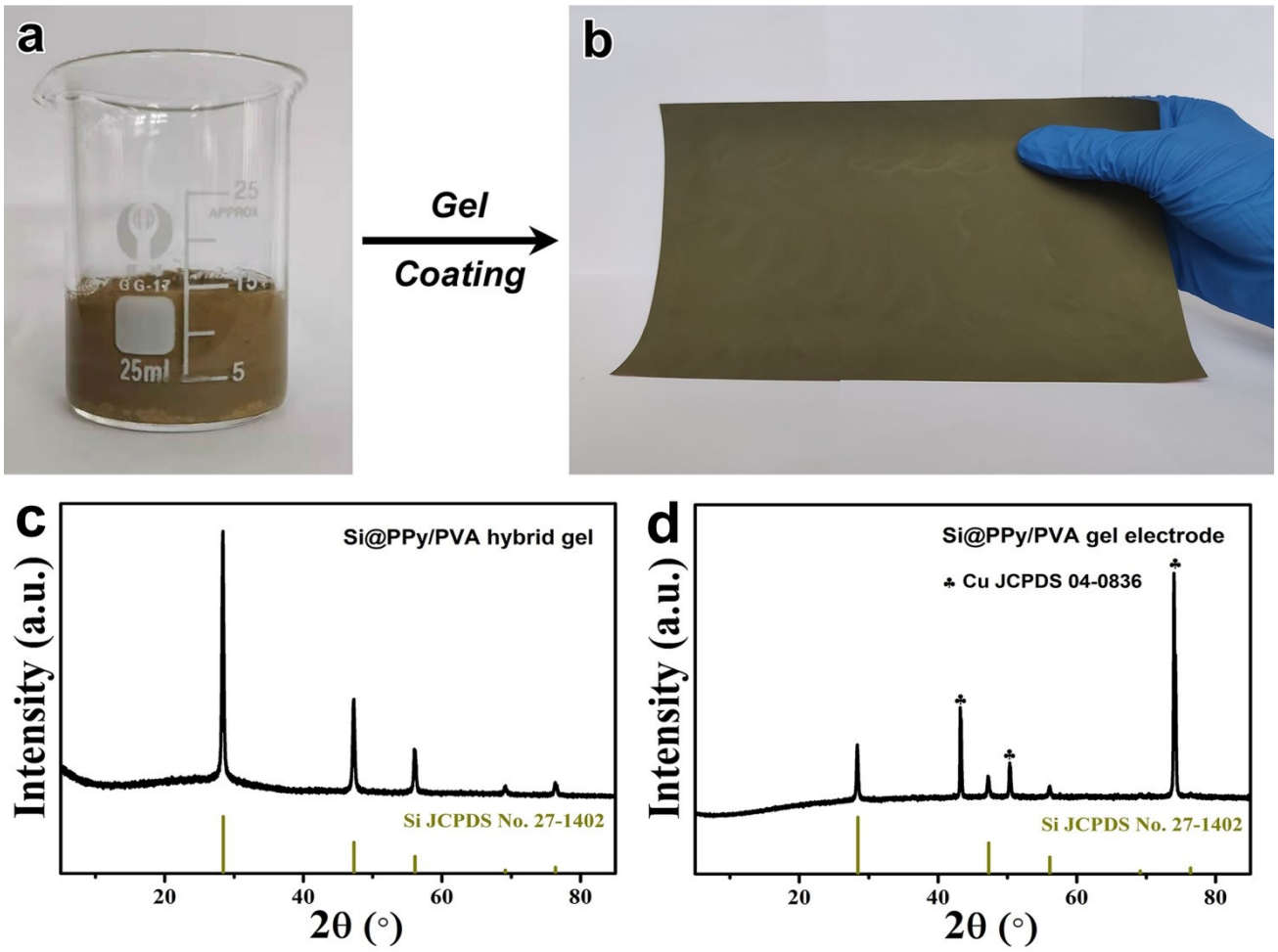

Fig. S12 The Si@PPy/PVA hybrid gel (a) has been spread on copper foil current collectors, yielding the Si@PPy/PVA gel electrode (b). XRD patterns of the Si@PPy/PVA hybrid gel (c) and Si@PPy/PVA gel electrode (d).

Fig. S12c and d reveal the XRD patterns of the Si@PPy/PVA hybrid gel and Si@PPy/PVA gel electrode. The characteristic diffraction peaks corresponding to cubic Si (JCPDS no. 27-1402) can be observed from both the patterns of the hybrid gel and gel electrode, whereas the PPy/PVA interpenetrating gel is amorphous in nature. Moreover, for the Si@PPy/PVA gel electrode, the additional diffraction peaks can be indexed to cubic Cu, which originate from copper foil current collectors.

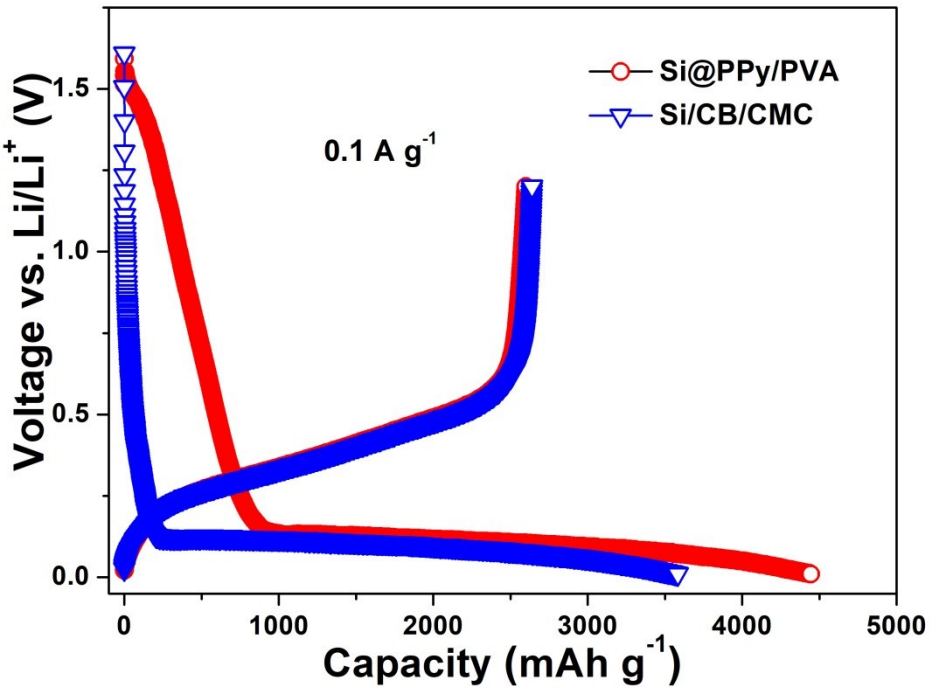

Fig. S13 The initial discharge and charge curves for the Si@PPy/PVA gel electrode in comparison with conventional electrode.

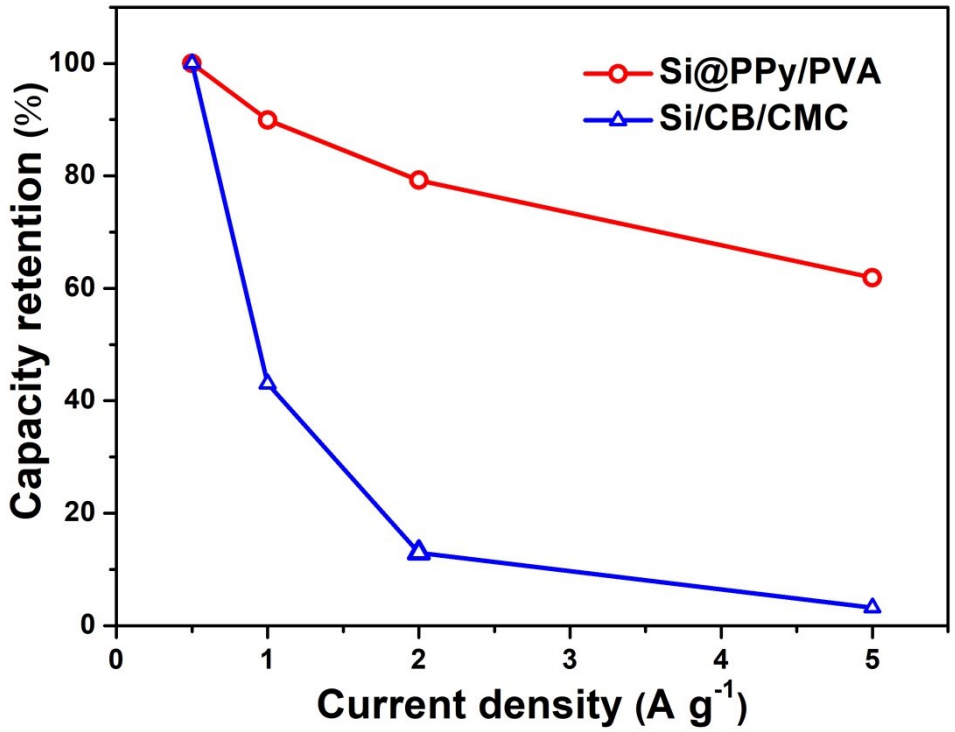

Fig. S14 Rate retention for the Si@PPy/PVA gel electrode in comparison with conventional electrode.

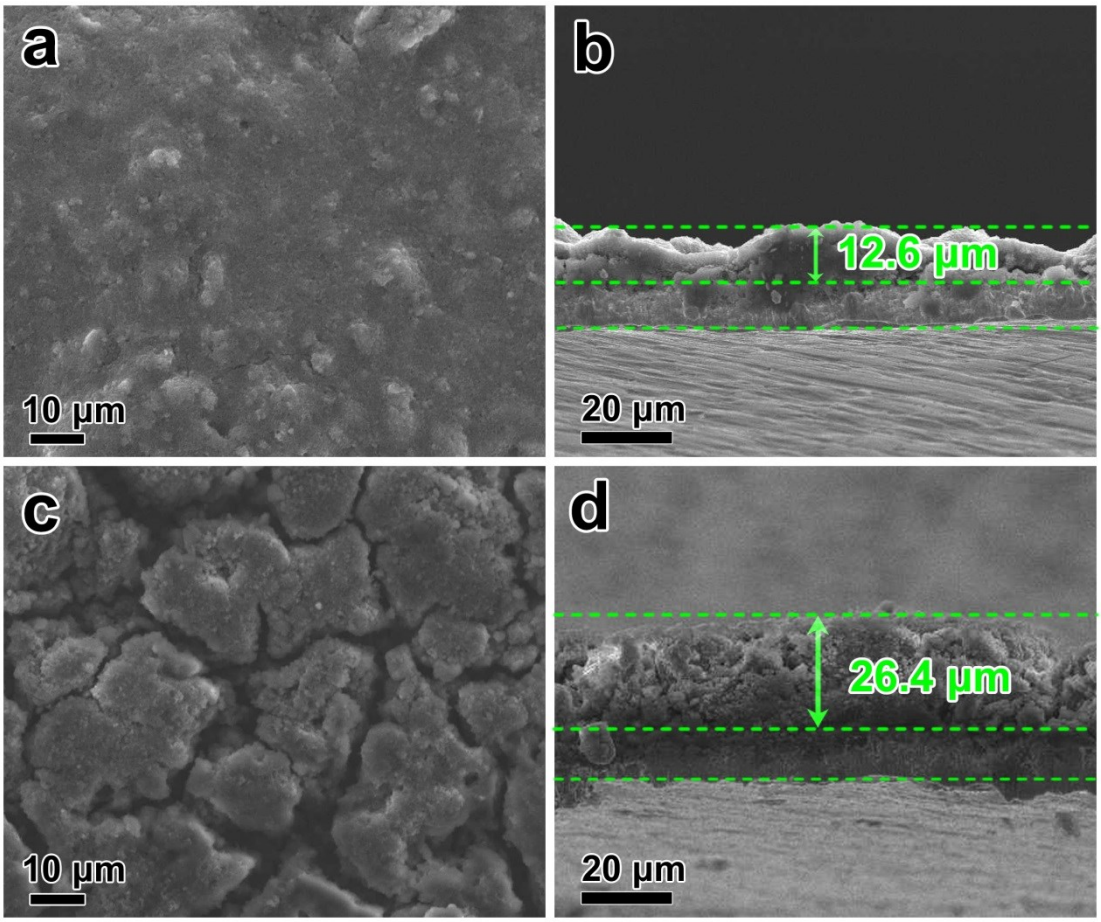

Fig. S15 Top and cross-sectional SEM images of the Si/CB/CMC conventional electrode before cycling (a, b) and after 100 cycles (c, d).

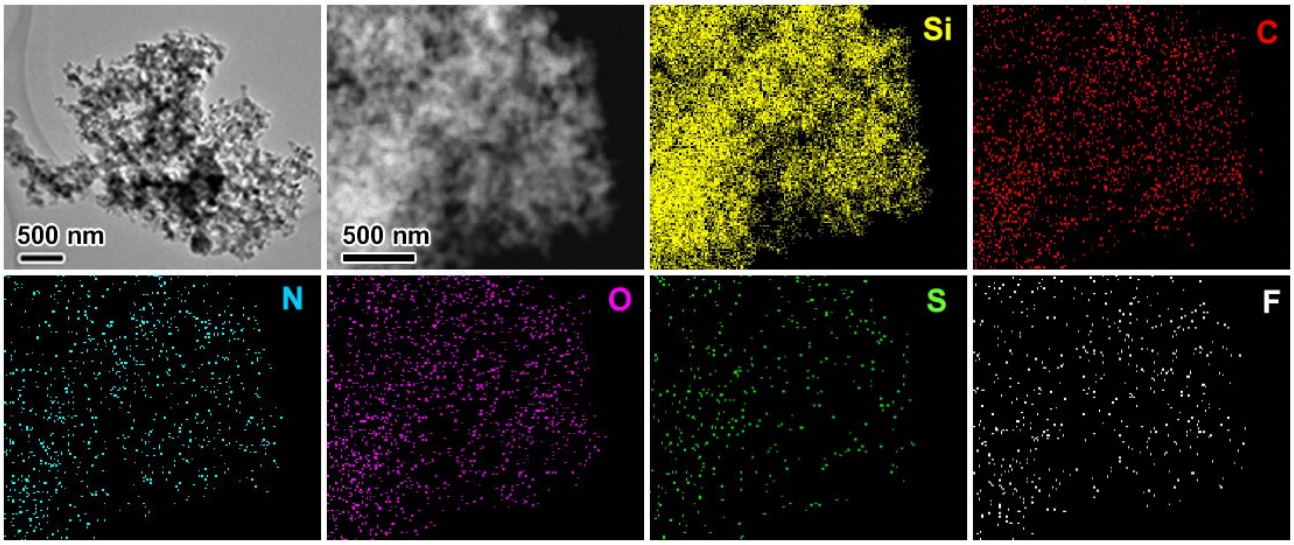

Fig. S16 TEM image and STEM-EDS elemental mappings of the Si@PPy/PVA gel electrode in a fully de-lithiated state (1.2 V *vs.* Li^+/Li) after 100 cycles.

Table S1 Comparison of the cycling stability and rate capability of the Si@PPy/PVA gel electrode with recently reported Si@polymer network electrodes.

Anode materials	Cycling stability ($mAh\ g^{-1}$)	Rate capability ($mAh\ g^{-1}$)	Ref
Si@PPy/PVA gel electrode	**1834 at 0.5 A g^{-1} (100 cycles)**	**1975 at 2 A g^{-1}** **1543 at 5 A g^{-1}**	**This work**
Si@CB/dextrin–GA electrode	~1430 at 0.42 A g^{-1} (100 cycles)	~1227 at 4.2 A g^{-1}	1
Si@CB/p(AA_{70}-co-nBA_{30})–PEGDE electrode	1220 at 0.5A g^{-1} (100 cycles)	~1800 at 1 A g^{-1}	2
Si@CB/PMDOPA electrode	~1580 at 0.84 A g^{-1} (100 cycles)	~1530 at 2.1 A g^{-1} ~1400 at 4.2 A g^{-1}	3
Si/PEDOT:PSS electrode	1950 at 1 A g^{-1} (100 cycles)	~1580 at 5 A g^{-1}	4
Si@CB/CMC–MAH electrode	~1070 at 1 A g^{-1} (100 cycles)	535 at 2 A g^{-1}	5
Si@CB/HPAM electrode	1639 at 0.358 A g^{-1} (100 cycles)	NA	6
Si@CB/CS–GA electrode	~1940 at 0.5 A g^{-1} (100 cycles)	~1950 at 2 A g^{-1}	7
Si@PANI/PAA electrode	~2350 at 0.84 A g^{-1} (100 cycles)	~1360 at 3.36 A g^{-1} ~590 at 6.72 A g^{-1}	8
Si@CB/PAA–SA electrode	~1005 at 0.2 A g^{-1} (100 cycles)	1632 at 0.8 A g^{-1}	9
Si@CB/ppSA–ppCMC electrode	~2080 at 0.5 A g^{-1} (100 cycles)	1720 at 2 A g^{-1} 1225 at 5 A g^{-1}	10

References

(1) S. Chen, H. Y. Ling, H. Chen, S. Zhang, A. Du and C. Yan, *J. Power Sources*, 2020, **450**, 227671.

(2) J. Son, T. N. Vo, S. Cho, A. N. Preman, I. T. Kim and S. Ahn, *J. Power Sources*, 2020, **458**, 228054.

(3) D. Yao, J. Feng, J. Wang, Y. Deng and C. Wang, *J. Power Sources*, 2020, **463**, 228188.

(4) T. M. Higgins, S. H. Park, P. J. King, C. Zhang, N. McEvoy, N. C. Berner, D. Daly, A. Shmeliov, U. Khan, G. Duesberg, V. Nicolosi and J. N. Coleman, *ACS Nano*, 2016, **10**, 3702–3713.

(5) P. Li, G. Chen, Y. Lin, F. Chen, L. Chen, N. Zhang, Y. Cao, R. Ma and X. Liu, *Macromol. Chem. Phys.*, 2020, **221**, 1900414.

(6) A. Miranda, X. Li, A. M. Haregewoin, K. Sarang, J. Lutkenhaus, R. Kostecki and R. Verduzco, *ACS Appl. Mater. Interfaces*, 2019, **11**, 44090–44100.

(7) C. Chen, S. H. Lee, M. Cho, J. Kim and Y. Lee, *ACS Appl. Mater. Interfaces*, 2016, **8**, 2658–2665.

(8) X. Wang, Y. Zhang, Y. Shi, X. Zeng, R. Tang and L. Wei, *Ionics*, 2019, **25**, 5323–5331.

(9) L. Zhu, F. Du, Y. Zhuang, H. Dai, H. Cao, J. Adkins, Q. Zhou and J. Zheng, *J. Electroanal. Chem.*, 2019, **845**, 22–30.

(10) R. Guo, S. Zhang, H. Ying, W. Yang, J. Wang and W. Han, *ChemSusChem*, 2019, **12**, 4838–4845.